Finite amplitude method applied to the giant dipole resonance in heavy rare-earth nuclei

Tomohiro Oishi,[1,2,*] Markus Kortelainen,[2,1] and Nobuo Hinohara[3,4]

[1]*Helsinki Institute of Physics, P.O. Box 64, FI-00014 University of Helsinki, Finland*
[2]*Department of Physics, P.O. Box 35 (YFL), University of Jyvaskyla, FI-40014 Jyvaskyla, Finland*
[3]*Center for Computational Sciences, University of Tsukuba, Tsukuba 305-8577, Japan*
[4]*FRIB Laboratory, Michigan State University, East Lansing, Michigan 48824, USA*

Background: The quasiparticle random phase approximation (QRPA), within the framework of nuclear density functional theory (DFT), has been a standard tool to access the collective excitations of atomic nuclei. Recently, the finite amplitude method (FAM) was developed in order to perform the QRPA calculations efficiently without any truncation on the two-quasiparticle model space.

Purpose: We discuss the nuclear giant dipole resonance (GDR) in heavy rare-earth isotopes, for which the conventional matrix diagonalization of the QRPA is numerically demanding. A role of the Thomas-Reiche-Kuhn (TRK) sum rule enhancement factor, connected to the isovector effective mass, is also investigated.

Methods: The electric dipole photoabsorption cross section was calculated within a parallelized FAM-QRPA scheme. We employed the Skyrme energy density functional self-consistently in the DFT calculation for the ground states and FAM-QRPA calculation for the excitations.

Results: The mean GDR frequency and width are mostly reproduced with the FAM-QRPA, when compared to experimental data, although some deficiency is observed with isotopes heavier than erbium. A role of the TRK enhancement factor in actual GDR strength is clearly shown: its increment leads to a shift of the GDR strength to higher-energy region, without a significant change in the transition amplitudes.

Conclusions: The newly developed FAM-QRPA scheme shows remarkable efficiency, which enables one to perform systematic analysis of GDR for heavy rare-earth nuclei. The theoretical deficiency of the photoabsorption cross section could not be improved by only adjusting the TRK enhancement factor, suggesting the necessity of an approach beyond self-consistent QRPA and/or a more systematic optimization of the energy density functional (EDF) parameters.

I. INTRODUCTION

Collective excitations of atomic nuclei reflect various properties of nuclear structure and the underlying interaction between nucleons. Their macroscopic or microscopic description has been a major subject in nuclear theory [1–6]. Recently, self-consistent mean-field models, based on nuclear density functional theory (DFT), have been intensively applied to the collective excitations in heavy open-shell nuclei, where *ab initio* models are still not computationally feasible.

The giant dipole resonance (GDR) is a noticeable phenomenon generated by electric dipole excitation. It is basically understood as a collective oscillation of all the neutrons against all the protons, occupying a major part of the nuclear giant resonances [1–4]. The GDR plays an essential role in the nuclear photoabsorption reaction, determining the centroid energy and width of the cross section. The nuclear photoabsorption reaction impacts also the dynamics of various astrophysical scenarios [7]. Therefore, GDR can provide a good testing ground for DFT-based theories to describe the nuclear collectivity, as well as the relevant physical properties of finite and infinite nuclear systems. For example, the centroid energy of GDR, which is well approximated as $\hbar\omega \cong 80A^{-1/3}$ MeV for spherical nuclei, can be connected to the symmetry

energy in infinite nuclear matter, which is an important pseudo-observable used to determine the parameters of the nuclear energy density functional (EDF) [6,8,9]. The wide spread of the GDR in neutron-rich nuclei [10] has been understood to originate from the ground state deformation, which has been well reproduced with modern nuclear EDFs [11–15]. Also, the pairing part of the nuclear EDF has been expected to play a significant role in the low-lying dipole excitations of exotic nuclei [16–20].

A commonly used DFT-based approach to address collective nuclear excitations is done in the framework of linear response theory, with the random-phase approximation (RPA). By taking the pairing correlations into account, the RPA is extended to the quasiparticle random-phase approximation (QRPA), which has been conventionally treated in the matrix formulation [5,21]. A fully self-consistent calculation within the matrix QRPA could be, however, numerically demanding due to the large size of QRPA matrices. Especially in the case where the spherical symmetry is broken, one often needs to employ an additional truncation on the two-quasiparticle model space in order to reduce the numerical cost [11,13,22,23]. Another approach to reduce the computational cost of the QRPA is the separable approximation for the residual interaction [15,24–26]. Such a truncation or approximation, however, may invoke spurious excitations due to the broken self-consistency between the Hartree-Fock-Bogoliubov (HFB) ground state and the QRPA solution.

---

*tomohiro.t.oishi@jyu.fi

The finite-amplitude method (FAM) provides an alternative way to solve the QRPA problem with a significantly reduced computational cost. With this method, the QRPA linear response problem is solved iteratively, by circumventing actual calculation and diagonalization of the QRPA matrix. FAM was originally developed for a computation of the RPA strength function, and soon after it was expanded to cover the QRPA problem within spherical symmetry [27,28]. In Ref. [29], FAM-QRPA was incorporated into the axially symmetric Skyrme-HFB solver, based on the harmonic oscillator basis. To date, FAM has been applied also to the axially symmetric coordinate-space HFB solver [30] and to the relativistic mean-field framework [31,32]. Various applications of the FAM include descriptions of giant and pygmy dipole excitations [33,34], efficient computation of the QRPA matrix elements [35], and evaluation of beta-decay rates, including the proton-neutron pairing correlations [36,37]. The contour integration technique of FAM-QRPA was developed to describe individual QRPA modes [38] and for a fast calculation of the energy-weighted sum rules [39]. In addition to FAM, the iterative Arnoldi method presents an alternative method to solve the QRPA problem iteratively [40]. It was also applied to the multipole excitations with pairing correlations [41,42].

This article is devoted to FAM-QRPA methodology applied to the GDR of the heavy rare-earth nuclei, within the Skyrme EDF framework. Due to the open-shell nature of these nuclei, pairing and deformation properties must be taken into account in a systematic study. We do not assume any truncation of the two-quasiparticle model space in the QRPA, nor the Bardeen-Cooper-Schrieffer (BCS) approximation for the pairing, but keep a full self-consistency between the HFB and QRPA. To check the validity of the FAM-QRPA, the results are compared with several sets of experimental data. We also investigate the impact of the Thomas-Reiche-Kuhn (TRK) sum rule enhancement factor on the isovector dipole excitation. Because the TRK sum rule is independent of theoretical models and only the enhancement factor (or equivalently, the isovector effective mass) includes information on the nuclear structure, the energy-weighted sum rule of GDR is an important quantity which reflects the properties of EDFs [5,8,9]. The sensitivity of GDR to the isovector effective mass is also discussed.

We introduce the basic formalism of the Skyrme EDF and FAM-QRPA in the next section. The results are presented and discussed in Sec. III. Finally, we summarize this article in Sec. IV.

II. FORMALISM

As a starting point, our HFB calculations were done in the Skyrme EDF framework. In order to write the Skyrme energy density, it is convenient to introduce the isoscalar and isovector local densities

$$\rho_0(\boldsymbol{r}) = \rho_n(\boldsymbol{r}) + \rho_p(\boldsymbol{r}), \quad \rho_1(\boldsymbol{r}) = \rho_n(\boldsymbol{r}) - \rho_p(\boldsymbol{r}), \quad (1)$$

where ρ_n and ρ_p are the neutron and proton densities. With these densities, the Skyrme energy density for the particle-hole

(ph) channel reads as

$$\mathcal{E}^{\text{Skyrme}} = \sum_{t=0,1} \left[\mathcal{E}_t^{\text{even}} + \mathcal{E}_t^{\text{odd}} \right], \quad (2)$$

$$\begin{aligned} \mathcal{E}_t^{\text{even}} = {} & C_t^{\rho\rho}[\rho_0]\rho_t^2 + C_t^{\rho\Delta\rho}\rho_t\Delta\rho_t + C_t^{\rho\tau}\rho_t\tau_t \\ & + C_t^{\rho\nabla J}\rho_t\nabla\cdot\boldsymbol{J}_t + C_t^{JJ}\sum_{\mu\nu}J_{\mu\nu,t}J_{\mu\nu,t}, \end{aligned} \quad (3)$$

$$\begin{aligned} \mathcal{E}_t^{\text{odd}} = {} & C_t^{ss}[\rho_0]\boldsymbol{s}_t^2 + C_t^{s\Delta s}\boldsymbol{s}_t\cdot\Delta\boldsymbol{s}_t + C_t^{sT}\boldsymbol{s}_t\cdot\boldsymbol{T}_t \\ & + C_t^{s\nabla j}\boldsymbol{s}_t\cdot(\nabla\times\boldsymbol{j}_t) + C_t^{jj}\boldsymbol{j}_t^2, \end{aligned} \quad (4)$$

where $t = 0\,(1)$ indicates the isoscalar (isovector) components. The time-even part $\mathcal{E}^{\text{even}}$ is a functional of the local density ρ, kinetic density τ, and spin-orbit densities $\boldsymbol{J}$ and $J_{\mu\nu,t}$, whereas the time-odd part $\mathcal{E}^{\text{odd}}$ is expressed with the spin density $\boldsymbol{s}$, current density $\boldsymbol{j}$, and kinetic-spin density $\boldsymbol{T}$. The detailed formulation of these quantities can be found in, e.g., Refs. [43,44]. The coupling coefficients $C_0^{\rho\rho}$, etc., are uniquely related to the well-known (t,x) parametrization of the Skyrme force [44,45]. Also, some of coupling constants can be connected to the properties of symmetric or asymmetric nuclear matter, which are useful pseudo-observables for optimization purposes of the Skyrme EDF parameters. These pseudo-observables can be treated as alternative EDF input parameters instead of coupling constants [46].

In the HFB calculation for the ground state of even-even nuclei, time-reversal symmetry is usually assumed, and hence the time-odd part of the functional does not make a contribution to the HFB solution. When the time-reversal symmetry becomes broken, like in the case of QRPA, the time-odd part becomes active. If we start from the original Skyrme force, the consequent time-odd part of the EDF has a unique correspondence to the time-even part. In other words, when we fix the coupling coefficients in the time-even part, those in the time-odd part should be automatically determined. In the EDF framework, however, a further generalization can be considered: one may treat the time-odd coefficients independently from the time-even ones. In this work, the time-odd part is determined as in the case of Skyrme force. For Coulomb energy density, the direct term is treated in the usual manner and for the exchange part we employ the Slater approximation.

For the particle-particle (pp) channel, which describes nuclear pairing correlations, we employ a functional of the density-dependent delta pairing (DDDP) energy density. That is,

$$\mathcal{E}^{\text{pair}} = \sum_{q=\text{n,p}} \frac{V_q^{\text{pair}}}{2} \left[1 - \zeta\frac{\rho_0(\boldsymbol{r})}{\rho_c} \right] \tilde{\rho}_q^2(\boldsymbol{r}), \quad (5)$$

where $\tilde{\rho}$ is the local pairing density and $\rho_c = 0.16\,\text{fm}^{-3}$ is the nuclear saturation density. In this article, a mixed DDDP ($\zeta = 1/2$) is adopted. The pairing strengths V_q^{pair} will be adjusted in Sec. III.

A. Finite amplitude method

The detailed formulation of FAM-(Q)RPA can be found in Refs. [27–29,38]. We briefly follow these works to arrange

the formalism necessary in this work. First, we assume an external time-dependent field, inducing a polarization on the HFB ground state. This external field is

$$\hat{\mathcal{F}}(t) = \eta[\hat{\mathcal{F}}e^{-i\omega t} + \hat{\mathcal{F}}^{\dagger}e^{i\omega t}],$$

$$\hat{\mathcal{F}} = \frac{1}{2}\sum_{\mu\nu}\left[F_{\mu\nu}^{20}(a_{\nu}a_{\mu})^{\dagger} + F_{\mu\nu}^{02}a_{\nu}a_{\mu}\right], \quad (6)$$

where $a_{\mu}^{\dagger}$ and a_{ν} are the quasiparticle creation and annihilation operators, respectively, and η is an infinitesimal real parameter. In this article, $\hat{\mathcal{F}}$ is assumed to be independent of ω, and restricted to have the form of the one-body operator. That is,

$$\hat{\mathcal{F}} = \sum_{kl} f_{kl}c_{k}^{\dagger}c_{l}, \quad (7)$$

where $c_{k}^{\dagger}$ and c_{l} are the original particle creation and annihilation operators. The expressions of $F_{\mu\nu}^{20}$ and $F_{\mu\nu}^{02}$ in terms of the Bogoliubov transformation can be found, e.g., in Refs. [5,28].

Time evolution of quasiparticles is described by the time-dependent HFB equation,

$$i\frac{\partial}{\partial t}a_{\mu}(t) = [\hat{\mathcal{H}}(t) + \hat{\mathcal{F}}(t), a_{\mu}(t)], \quad (8)$$

where the deviation from the static HFB solution is represented as

$$a_{\mu}(t) = e^{iE_{\mu}t}[a_{\mu} + \delta a_{\mu}(t)],$$

$$\delta a_{\mu}(t) = \eta\sum_{\nu}a_{\nu}^{\dagger}[X_{\nu\mu}(\omega)e^{-i\omega t} + Y_{\nu\mu}^{*}(\omega)e^{i\omega t}]. \quad (9)$$

The quantities needed to obtain the multipole transition strength are the FAM amplitudes, $X_{\nu\mu}(\omega)$ and $Y_{\nu\mu}(\omega)$, at the excitation energy ω. Since the external field induces density oscillations atop of the static HFB density, the self-consistent Hamiltonian also contains an induced oscillation: $\hat{\mathcal{H}}(t) = \hat{\mathcal{H}}_{\text{HFB}} + \delta\hat{\mathcal{H}}(t)$, where

$$\delta\hat{\mathcal{H}}(t) = \eta[\delta\hat{\mathcal{H}}e^{-i\omega t} + \delta\hat{\mathcal{H}}^{\dagger}e^{i\omega t}],$$

$$\delta\hat{\mathcal{H}} = \frac{1}{2}\sum_{\mu\nu}\left[\delta H_{\mu\nu}^{20}(\omega)(a_{\nu}a_{\mu})^{\dagger} + \delta H_{\mu\nu}^{02}(\omega)a_{\nu}a_{\mu}\right]. \quad (10)$$

Solving Eq. (8) up to the first order in η yields the so-called FAM equations

$$[E_{\mu} + E_{\nu} - \omega]X_{\mu\nu}(\omega) + \delta H_{\mu\nu}^{20}(\omega) = -F_{\mu\nu}^{20},$$

$$[E_{\mu} + E_{\nu} + \omega]Y_{\mu\nu}(\omega) + \delta H_{\mu\nu}^{02}(\omega) = -F_{\mu\nu}^{02}. \quad (11)$$

It is worthwhile to note that, by using the expressions of $\delta H_{\mu\nu}^{20}(\omega)$ and $\delta H_{\mu\nu}^{02}(\omega)$ in terms of $X_{\mu\nu}(\omega)$ and $Y_{\mu\nu}(\omega)$, one can transform Eq. (11) into the matrix form of

$$\left[\begin{pmatrix} A & B \\ B^{*} & A^{*} \end{pmatrix} - \omega\begin{pmatrix} \mathbf{1} & 0 \\ 0 & -\mathbf{1} \end{pmatrix}\right]\begin{pmatrix} X(\omega) \\ Y(\omega) \end{pmatrix} = -\begin{pmatrix} F^{20} \\ F^{02} \end{pmatrix}, \quad (12)$$

where A and B are the well-known QRPA matrices [5]. Notice that Eq. (12) yields the standard matrix form of QRPA when the external field is set to zero. The solution of Eq. (12), however, would require us to compute the QRPA matrices A and B which generally have large dimensions, leading to a substantial CPU time requirement. The essential trick of the FAM-QRPA

is to keep Eq. (11) and to solve the FAM amplitudes iteratively with respect to the response of the self-consistent Hamiltonian. This allows us to circumvent the large numerical cost of matrix QRPA.

The response of the self-consistent Hamiltonian, $\delta H_{\mu\nu}^{20}(\omega)$ and $\delta H_{\mu\nu}^{02}(\omega)$, can be expressed in terms of the induced fields,

$$\delta H_{\mu\nu}^{20}(\omega) = \{U^{\dagger}\delta h(\omega)V^{*} - V^{\dagger}\delta h(\omega)^{T}U^{*}$$
$$- V^{\dagger}\overline{\delta\Delta}(\omega)^{*}V^{*} + U^{\dagger}\delta\Delta(\omega)U^{*}\}_{\mu\nu},$$

$$\delta H_{\mu\nu}^{02}(\omega) = \{U^{T}\delta h(\omega)^{T}V - V^{T}\delta h(\omega)U$$
$$- V^{T}\delta\Delta(\omega)V + U^{T}\overline{\delta\Delta}(\omega)^{*}U\}_{\mu\nu}. \quad (13)$$

with the well-known HFB matrices U and V. Originally the induced FAM-QRPA fields, δh, $\delta\Delta$, and $\overline{\delta\Delta}$, were calculated by applying numerical functional derivatives. In Ref. [47], on the other hand, these fields were obtained through explicit linearization of the Hamiltonian, in order not to mix the densities with different magnetic quantum numbers K. Thanks to this explicit linearization, the infinitesimal parameter η is no longer needed, and the induced fields can be formulated in a manner similar to the HFB fields. That is, $\delta h(\omega) = h'[\rho_{f}, \kappa_{f}, \overline{\kappa}_{f}]$, $\delta\Delta(\omega) = \Delta'[\rho_{f}, \kappa_{f}]$, and $\overline{\delta\Delta}(\omega) = \Delta'[\overline{\rho}_{f}, \overline{\kappa}_{f}]$, where h' and Δ' are the linearized fields with respect to perturbed densities. These densities can be expressed as

$$\rho_{f}(\omega) = +UX(\omega)V^{T} + V^{*}Y(\omega)^{T}U^{\dagger},$$

$$\overline{\rho}_{f}(\omega) = +V^{*}X(\omega)^{\dagger}U^{\dagger} + UY(\omega)^{*}V^{T},$$

$$\kappa_{f}(\omega) = -UX(\omega)^{T}U^{T} - V^{*}Y(\omega)V^{\dagger},$$

$$\overline{\kappa}_{f}(\omega) = -V^{*}X(\omega)^{*}V^{\dagger} - UY(\omega)^{\dagger}U^{T}. \quad (14)$$

The procedures that provide h and Δ for the HFB solution can be also utilized for the linearized fields, h' and Δ', with a minor modification. For an iterative solution of the FAM amplitudes, the Broyden method was utilized to obtain a rapid convergence [48,49].

By using the FAM-QRPA amplitudes obtained through the iteration, the multipole transition strength distribution is expressed as

$$\frac{dB(\hat{\mathcal{F}};\omega)}{d\omega} \equiv \sum_{i>0}|\langle i|\hat{\mathcal{F}}|0\rangle|^{2}\delta(\omega - \Omega_{i})$$

$$= -\frac{1}{\pi}\text{Im }S(\hat{\mathcal{F}};\omega), \quad (15)$$

where $i > 0$ denotes the summation over the states with positive QRPA energies $\Omega_{i} > 0$, and the response function is given by $S(\hat{\mathcal{F}};\omega) = \text{tr}[f\rho_{f}]$ [28,47]. In order to prevent the FAM-QRPA strength from diverging at $\omega = \Omega_{i}$, we employ a small imaginary part in the energy, $\omega \rightarrow \omega_{\gamma} = \omega + i\gamma$, corresponding to a Lorentzian smearing of $\Gamma = 2\gamma$ [28]. The explicit formulation of this smeared strength can be found in Ref. [38]:

$$S(\hat{\mathcal{F}};\omega_{\gamma}) = -\sum_{i>0}\left(\frac{|\langle i|\hat{\mathcal{F}}|0\rangle|^{2}}{\Omega_{i} - \omega - i\gamma} + \frac{|\langle 0|\hat{\mathcal{F}}|i\rangle|^{2}}{\Omega_{i} + \omega + i\gamma}\right). \quad (16)$$

The contour integration technique is worth mentioning: discrete QRPA amplitudes or various multipole sum rules can be obtained from $S(\hat{\mathcal{F}}; \omega_\gamma)$ with a suitable selection of the integration contour on a complex (ω, γ) plane [38,39].

We use following external fields to compute the electric isovector dipole (IVD) strength $dB(\hat{\mathcal{D}}_K; \omega)/d\omega$:

$$\hat{\mathcal{F}} = \hat{\mathcal{D}}_K \quad (K = 0, \pm 1),$$

$$\hat{\mathcal{D}}_K = e\frac{NZ}{A}\left[\sum_{i \in N} \frac{-1}{N} D_K(\boldsymbol{r}_i) + \sum_{j \in Z} \frac{1}{Z} D_K(\boldsymbol{r}_j)\right],$$

with $D_K(\boldsymbol{r}) = rY_{1K}(\bar{\boldsymbol{r}})$. In actual calculation, we replace this operator as

$$D_K \rightarrow D_K^+ = (D_K + D_{-K})/\sqrt{2 - \delta_{0K}}. \quad (17)$$

Indeed, for an even-even axial nucleus, D_K and D_{-K} yield an identical transition strength.

III. RESULTS AND DISCUSSIONS

A. Benchmark calculation

The HFB calculations were done using the SkM* Skyrme parametrization at the ph channel [50]. This set of parameters has been confirmed to be stable in the linear response calculation for infinite nuclear matter [51]. Since SkM* lacks tensor terms, corresponding time-odd terms were also excluded. For the pp channel, the pairing strengths for neutrons and protons were adjusted to reproduce empirical pairing gaps of ^{156}Dy: $V_n^{\text{pair}} = -282.0$ MeV fm^3 and $V_p^{\text{pair}} = -307.9$ MeV fm^3. The pairing cutoff window needed for the DDDP is fixed to 60 MeV. We use computer code HFBTHO, which is an HFB solver based on the harmonic oscillator (HO) basis within the axial symmetry [52]. The imaginary part of ω_γ for the FAM strength was set to $\gamma = 0.5$ MeV, corresponding to a smearing width of $\Gamma = 1.0$ MeV, unless otherwise stated.

We would like to emphasize that, in contrast to the standard solution of the QRPA by matrix diagonalization (MQRPA), no truncations on the QRPA quasiparticle model space are imposed in our FAM-QRPA scheme. The only cutoffs employed are the number of HO shells and the pairing window; thus, self-consistency between the HFB and QRPA is fully maintained.

Figure 1 shows a benchmark result of FAM-QRPA applied to the GDR. Here we plotted the photoabsorption cross sections obtained with the IVD strengths for ^{144,154}Sm:

$$\sigma_{\text{abs}}(\omega) = \frac{4\pi^2}{\hbar c}\omega \sum_{K=0,\pm 1} \frac{dB(\hat{\mathcal{D}}_K; \omega)}{d\omega}. \quad (18)$$

The quadrupole matter distribution deformations of the HFB ground states are $\beta = 0$ and 0.317 for ^{144}Sm and ^{154}Sm, respectively. The IVD strengths of the $K = 0$ and $|K| = 1$ modes split in ^{154}Sm due to the ground state deformation, whereas those are identical for spherical ^{144}Sm. In both cases, FAM-QRPA shows a good agreement with the experimental data [53]: the typical frequency and width of the GDR can be well reproduced with our model parameters, with the smearing width of $\Gamma = 1.0$ MeV. The plateau distribution

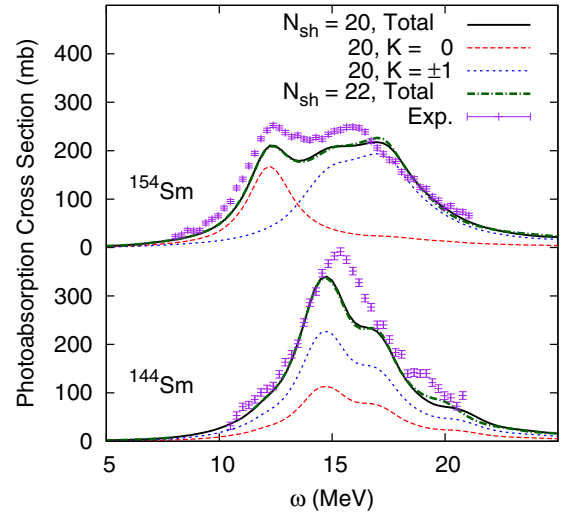
FIG. 1. Photoabsorption cross sections of ^{144,154}Sm from the FAM-QRPA calculation with 20 harmonic oscillator shells. The components from the $K = 0$ and $K = \pm 1$ modes are separately plotted, where $K = \pm 1$ refers to a sum of $+1$ and -1 modes. The total photoabsorption cross section, calculated with 22 oscillator shells, is also included in the plot. The experimental data are taken from Ref. [53].

for the deformed ^{154}Sm can be understood as a product of the split between $K = 0$ and $|K| = 1$ modes [13,14]. Our result also shows a good consistency with that of Ref. [13], in which MQRPA within the coordinate-space representation was adopted.

In this work, we have used a HO basis consisting of 20 major oscillator shells. We have confirmed that our results are well converged by comparing to the photoabsorption cross section computed with 22 oscillator shells, as shown in Fig. 1. Employing more shells provides only a minor modification of the photoabsorption cross sections, and this effect is negligibly small compared with uncertainties originating from the used EDF parametrization itself.

We have computed the FAM strength function within the MPI parallelized scheme, where each part of the strength function was distributed on a separate core, similarly to the method in Ref. [47]. This scheme achieves a remarkable efficiency, enabling us to compute deformed heavier systems, where MQRPA is available only with a truncation of the model space. Typically, a computation of both of the K modes took about 1500 CPU hours in a multicore Intel Sandy Bridge 2.6-GHz processor system.

B. GDR in heavy rare-earth nuclei

Our survey of the GDR has been performed for even-even rare-earth nuclei from Gd ($Z = 64$) to W ($Z = 74$) isochains. Because several sets of experimental data are available [54–56], they can provide a more systematic check for FAM-QRPA GDR results. In Tables I and II, we summarize the ground state properties of computed nuclei. The HFB calculation with SkM* concludes that all the nuclei considered here have rather stable prolate deformation.

TABLE I. Ground state properties of Gd, Dy, and Er isotopes obtained with the SkM* parametrization: axial deformation β, pairing gaps for neutrons and protons (Δ_n, Δ_p), energy-weighted sum rule from Eq. (21), $m_1(\hat{\mathcal{D}}_K)$, and its enhancement factor from the TRK sum rule κ^{IVD} (For SkM*, $\kappa^{\mathrm{NM}} = 0.5315$).

Nuclide	β	Δ_n, Δ_p (MeV)]	$m_1(\hat{\mathcal{D}}_K)$ ($e^2\mathrm{fm}^2\mathrm{MeV}$)	κ^{IVD}
^{152}Gd	0.235	1.09,1.19	253.9	0.3939
^{154}Gd	0.301	1.16,0.97	256.5	0.3944
^{156}Gd	0.331	1.08,0.89	258.9	0.3950
^{158}Gd	0.346	1.05,0.84	261.3	0.3953
^{160}Gd	0.355	1.04,0.80	263.6	0.3955
^{162}Gd	0.358	1.07,0.78	265.8	0.3955
^{164}Gd	0.358	1.06,0.76	267.9	0.3954
^{156}Dy	0.289	1.17,0.98	261.1	0.3944
^{158}Dy	0.320	1.13,0.88	263.7	0.3949
^{160}Dy	0.336	1.10,0.82	266.1	0.3954
^{162}Dy	0.344	1.09,0.78	268.5	0.3956
^{164}Dy	0.347	1.09,0.73	270.8	0.3957
^{166}Dy	0.349	1.06,0.69	273.0	0.3958
^{168}Dy	0.348	1.01,0.67	275.2	0.3959
^{162}Er	0.324	1.15,0.87	270.8	0.3953
^{164}Er	0.334	1.14,0.81	273.3	0.3957
^{166}Er	0.339	1.12,0.75	275.7	0.3959
^{168}Er	0.342	1.08,0.70	278.1	0.3962
^{170}Er	0.342	1.00,0.65	280.4	0.3964
^{172}Er	0.337	0.97,0.63	282.6	0.3965
^{174}Er	0.329	1.06,0.61	284.7	0.3964

Our results from FAM-QRPA are summarized in Figs. 2 and 3, in which the photoabsorption cross sections are compared with experimental data, where available. We emphasize here that experimental data in Refs. [56–58] do not correspond

TABLE II. The same as Table I but for Yb, Hf, and W isotopes.

| Nuclide	β	Δ_n, Δ_p (MeV)	$m_1(\hat{\mathcal{D}}_K)$ ($e^2\mathrm{fm}^2\mathrm{MeV}$)	κ^{IVD}
^{168}Yb	0.331	1.16,0.60	280.5	0.3961
^{170}Yb	0.335	1.10,0.37	283.0	0.3966
^{172}Yb	0.336	1.01,0	285.4	0.3970
^{174}Yb	0.332	0.94,0	287.7	0.3973
^{176}Yb	0.324	1.01,0	289.9	0.3972
^{178}Yb	0.315	1.08,0	292.0	0.3970
^{174}Hf	0.326	1.00,0.85	290.1	0.3965
^{176}Hf	0.316	0.97,0.80	292.5	0.3970
^{178}Hf	0.301	1.03,0.74	294.8	0.3971
^{180}Hf	0.288	1.06,0.68	297.1	0.3970
^{182}Hf	0.276	1.06,0.64	299.2	0.3969
^{184}Hf	0.263	1.03,0.62	301.4	0.3969
^{180}W	0.270	1.09,0.80	299.7	0.3971
^{182}W	0.257	1.11,0.73	302.0	0.3972
^{184}W	0.245	1.10,0.68	304.3	0.3972
^{186}W	0.230	1.07,0.66	306.5	0.3973
^{188}W	0.212	1.01,0.65	308.7	0.3974
^{190}W	0.191	0.97,0.66	310.9	0.3974
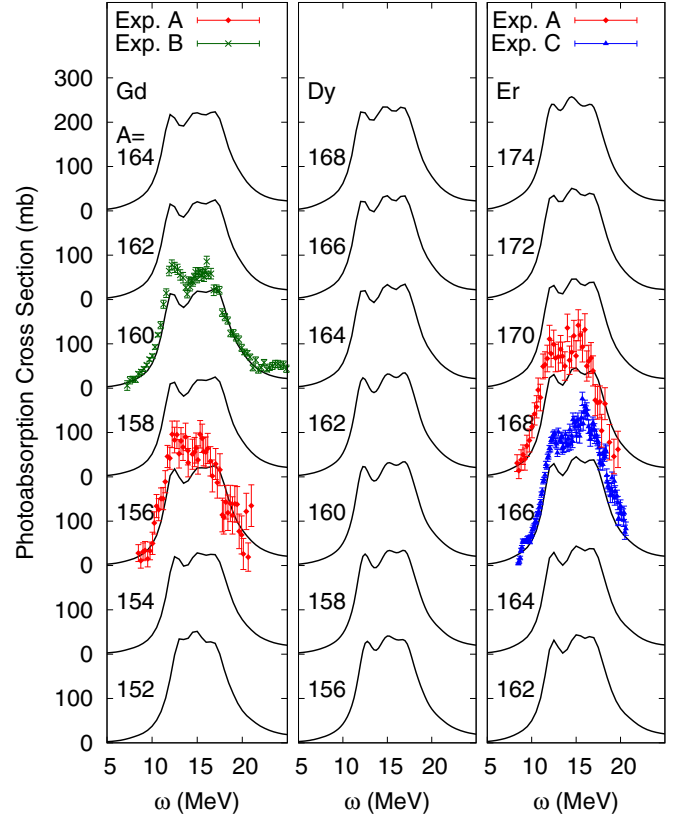
FIG. 2. Photoabsorption cross sections of Gd, Dy, and Er isotopes as a function of photon energy. For the FAM-QRPA calculation, the smearing width $\Gamma = 1.0$ MeV is used. The experimental data sets A, B (photoabsorption), and C (neutron yield) are taken from Refs. [54–56], respectively.

to the total photoabsorption cross section, but the photoneutron cross sections of (γ,n) and $(\gamma,2n)$ types of reactions. Thus, the data include only a part of total photoabsorption cross section due to smaller number of output channels. Generally, we find a reasonable agreement between the FAM-QRPA and the experiments. Typical frequencies of GDR are fairly well reproduced throughout the rare-earth isotopes heavier than Sm. The width and the plateau top of the distribution are well understood as a product from the splitting of $K = 0$ and $|K| = 1$ modes, corresponding to the prolate deformation commonly found on their ground states. For ^{152}Gd and several isotopes of W, the width of the GDR is graphically narrower than other nuclei, as expected due to smaller prolate deformation. In our HFB calculations, the proton pairing collapses for $^{172-178}$Yb. This collapse itself, however, does not make a significant impact on the GDR, as the GDR strength distributions look similar irrespective of the proton pairing collapse. Although the pairing could affect the GDR indirectly through the ground state properties (mainly deformation), their changes are small among the rare-earth nuclei, as shown in the present study.

There is an observed deficiency in the calculated photoabsorption cross sections at the region of heavier rare-earth isotopes, namely for $Z \geqslant 70$. For example, the calculated photoabsorption cross section of ^{174}Yb underestimates the experimental data of Ref. [54] in the region $\omega = 12$–17 MeV,
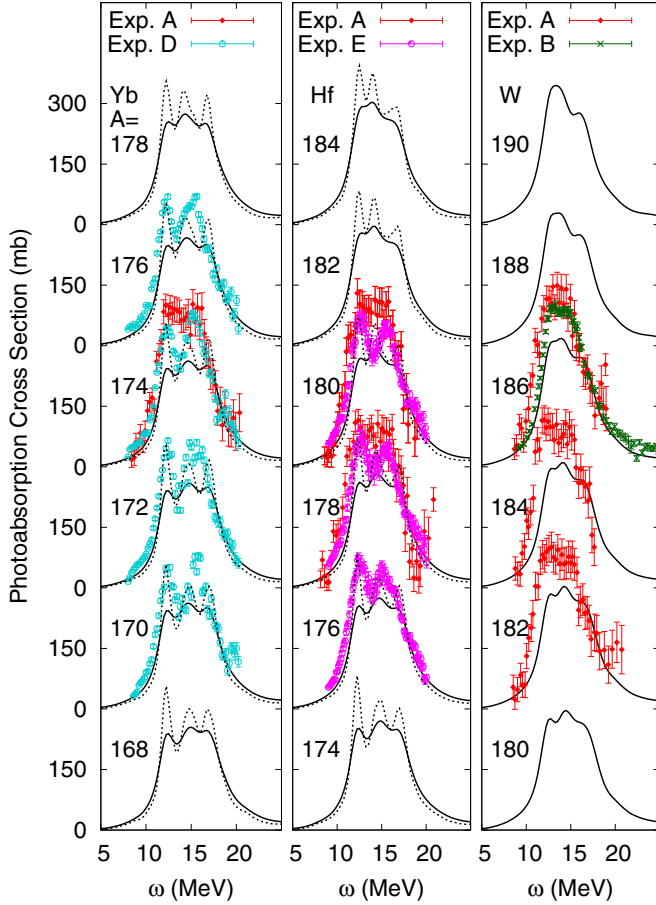
FIG. 3. The same as Fig. 2 but for Yb, Hf, and W isotopes. The experimental data sets A, B (photoabsorption), D (neutron yield), and E (neutron product) are taken from Refs. [54,55,57,58], respectively. For Yb and Hf, the results obtained with the smearing width of $\Gamma = 0.5$ MeV are also plotted with dotted lines.

FIG. 4. Photoabsorption cross sections of ^{174}Yb obtained with different values of the smearing width Γ. The shown experimental data are the same as those in Fig. 3.

in which GDR becomes noticeably strong. A similar kind of GDR deficiency with Skyrme EDFs was reported in Ref. [59].

In Fig. 3, we have also plotted results for the Yb and Hf isotopes by using a smaller smearing width: $\Gamma = 0.5$ MeV. With this smaller width, we can reproduce the cross section of the neutron yield up to $\omega \approx 13$ MeV, which includes the first peak of the experimental data of Refs. [57,58]. The second peak of the neutron yield cross section may be attributable to the opening of the two-neutron emission channel: for ^{174}Yb, for example, that peak is located at $\omega = 15$ MeV, which is just above the two-neutron separation energy. With $\Gamma = 0.5$ MeV, however, we could not achieve a complete improvement of aforementioned deficiency, and the total photoabsorption cross section remains underestimated. In Fig. 4, we also show that the narrower width of $\Gamma = 0.3$ MeV leads computed photoabsorption cross sections to overshoot the experimental values at the peak positions, whereas a discrepancy at other frequencies remains. Consequently, the GDR deficiency found here is not improved by simply changing the smearing parameter Γ. Further systematic experiments of photoabsorption cross section, with improved accuracy, would be helpful by
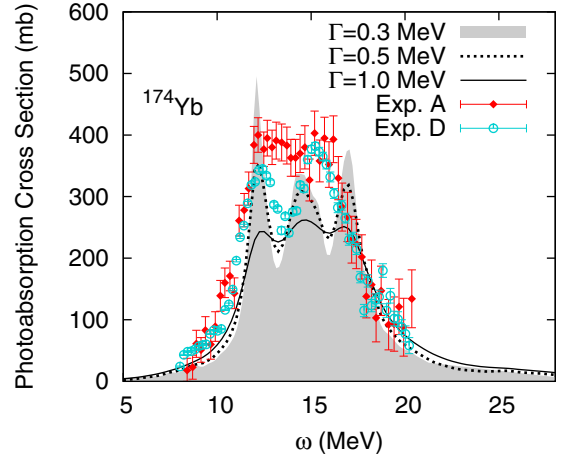
providing a more complete testing ground for theoretical models.

Theoretical deficiency of the GDR may be connected to the essential properties of the model. In order to remedy this deficiency, one could consider, e.g., beyond-QRPA effects or systematic adjustment of the EDF parameters. These are, however, beyond the scope of this article. Alternatively, we discuss a role of the TRK sum rule enhancement factor κ^{IVD} and its role in the isovector dipole excitation [8,9]. This quantity can be related to the isovector effective mass of infinite nuclear matter (INM), which can be used as an input parameter to define the Skyrme EDF parameters [46]. Because there has been some ambiguity about the empirical value of this parameter, knowledge of its effect on GDR will be also profitable for the future optimization of the EDF parameters.

C. Energy-weighted sum rule

To discuss the sensitivity of GDR to the model parameters, we investigate the energy-weighted sum rule (EWSR), defined as

$$m_1(\hat{\mathcal{D}}_K) = \int \omega \frac{dB(\hat{\mathcal{D}}_K;\omega)}{d\omega} d\omega. \tag{19}$$

In terms of the transition matrix elements, it can be rewritten as

$$m_1(\hat{\mathcal{D}}_K) = \sum_{i>0} \Omega_i |\langle i|\hat{\mathcal{D}}_K|0\rangle|^2. \tag{20}$$

It is well known that, by applying the Thouless theorem [60], the EWSR based on the QRPA can be replaced with the expectation value of the double commutator of the HFB ground state [61,62]. For the present case this reads as

$$m_1(\hat{\mathcal{D}}_K) = \frac{1}{2}\langle 0|[\hat{\mathcal{D}}_K,[\hat{H},\hat{\mathcal{D}}_K]]|0\rangle$$

$$= (1 + \kappa^{\mathrm{IVD}})\frac{e^2\hbar^2}{2m}\frac{NZ}{A}\frac{3}{4\pi}, \tag{21}$$

where κ^{IVD} is the enhancement factor due to the momentum dependence of the effective interaction. For the Skyrme force, it can be given as

$$\kappa^{IVD} = \frac{2m}{\hbar^2}\left(C_0^{\rho\tau} - C_1^{\rho\tau}\right)\frac{A}{NZ}\int \rho_n(\boldsymbol{r})\rho_p(\boldsymbol{r})d\boldsymbol{r}. \qquad (22)$$

For the IVD mode, the EWSR has the same value for $K = 0$ and 1 cases, even if the ground state is deformed. Note also that, for INM, $\kappa^{NM} = 2m(C_0^{\rho\tau} - C_1^{\rho\tau})\rho_c/\hbar^2$ is obtained.

Before going to applications, we check the validity of Eq. (21) in a generalized EDF framework [39]. When the EDF is formally generalized, and has no correspondence with respect to the underlying effective force, the Thouless theorem is not guaranteed to remain valid. Because we employed the Skyrme EDF combined with the mixed DDDP, the EWSR from actual QRPA calculations can deviate from Eq. (21). In Ref. [39], the authors showed that the Thouless theorem provides a reasonable approximation to the EWSR of the isoscalar/isovector monopole and quadrupole modes, even when Skyrme EDF lacks exact correspondence with respect to the underlying effective interaction but still holds the local gauge invariance. Here we give a similar test for the IVD mode.

For ^{174}Yb, the energy-weighted sum rule, integrated directly from the transition strength function up to $\omega = 50$ MeV, yields $m_1(\hat{\mathcal{D}}_K) = 282.7$ and 282.1 e^2 fm^2 MeV for $K = 0$ and $K = 1$ modes, respectively. Because of the deformation and the resultant splitting of $K = 0$ and $K = 1$ strengths, there is a small difference between the two values. The contour integration technique of the complex-energy FAM, developed as an efficient tool to compute the sum rules in Ref. [39], yields $m_1(\hat{\mathcal{D}}_{K=0}) = 288.0$ e^2 fm^2 MeV with an integration contour radius of 200 MeV. On the other hand, the double commutator procedure of Eq. (21) gives $m_1(\hat{\mathcal{D}}_{K=0,\pm1}) = 287.7$ e^2 fm^2 MeV, with enhancement factor of $\kappa^{IVD} = 0.397$, when using HFB proton and neutron densities.

We find the value from the double commutator method being consistent with those from the FAM-QRPA calculation. Consequently, the Thouless theorem can provide a reliable approximation of the IVD sum rule. The computational cost for the double commutator procedure is drastically lighter compared to the FAM-QRPA, since it requires information only about the HFB state.

We have summarized the EWSR values and enhancement factors of Eqs. (21) and (22) in Tables I and II. It is clearly shown that the enhancement factor for the TRK sum rule is almost constant in this region of the nuclear chart. The ratio of two enhancement factors,

$$\frac{\kappa^{IVD}}{\kappa^{NM}} = \frac{A}{NZ\rho_c}\int \rho_n(\boldsymbol{r})\rho_p(\boldsymbol{r})d\boldsymbol{r}, \qquad (23)$$

is approximately 0.74 for rare-earth systems calculated here with the SkM* Skyrme parametrization. This is simply due to the similar value obtained from the density integration of Eq. (23), with only a limited variation on the proton and neutron density profiles with respect of N and Z.

In Fig. 5, we plot the enhancement factor κ^{IVD} and the total HFB energy E_{HFB} as functions of the axial deformation parameter β for ^{174}Yb. These are obtained from the HFB calculation with a constraint on β. Approximately, the
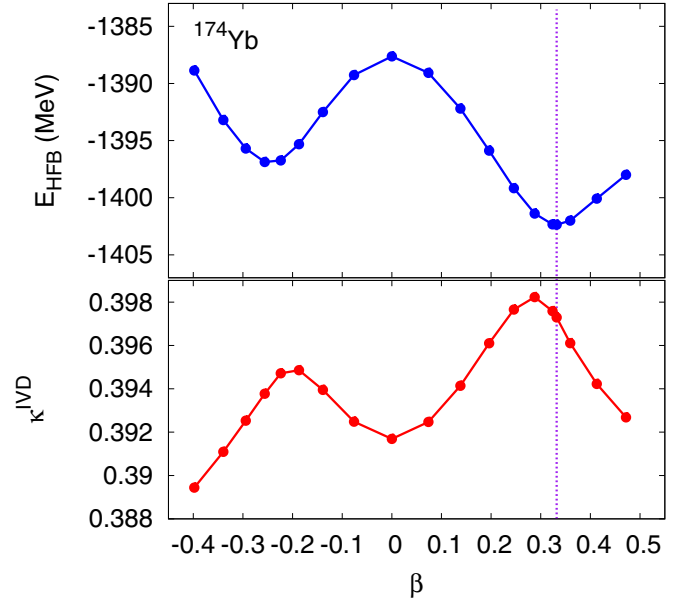

FIG. 5. The total HFB energy and the IVD enhancement factor of ^{174}Yb as functions of the axial deformation. The HFB ground state is indicated by the vertical dotted line.

minimum of the total HFB energy corresponds to the maximum of κ^{IVD}. This can be understood mainly in terms of the symmetry energy, which favors a large overlap between neutrons and protons. Due to other ingredients, especially the Coulomb energy, the true ground state and maximum of κ^{IVD} do not exactly coincide. This curve shows, however, that the IVD enhancement factor is not very sensitive to the details of the ground state deformation. Next, we investigate if the deficiency against the experimental photoabsorption data found in ^{174}Yb could be improved by changing the κ^{NM} parameter.

D. Sensitivity to enhancement factor

In the remaining part of this section, we investigate the sensitivity of GDR to the EDFs with different κ^{NM} values. The Skyrme parametrizations suited to this purpose can be found in Ref. [44], where the authors optimized Skyrme parameters by assuming systematic constraints on various INM properties. The unconstrained parametrization, SV-min, was optimized without constraints, and the SV-bas parametrization was a base starting point for INM parameter variation. The parametrizations with a variation on κ^{NM} were introduced as SV-kap60 and SV-kap20. Because these constrained parametrizations were otherwise optimized exactly in the same manner as SV-bas, we can check the effect of κ^{NM} on the GDR in a systematic manner. The exact value of κ^{NM} as an input parameter for each functional is present in Table III. Note that the larger value of the enhancement factor corresponds to the lighter isovector effective mass ($\kappa^{NM} = m/m_v^* - 1$) [9,44]. Except for the interaction parametrization employed, the numerical conditions are the same as in the previous calculations.

In Table III, the EWSR of ^{174}Yb obtained with SkM*, SV-kap20, SV-bas, and SV-kap60 are summarized with the corresponding enhancement factors. As naturally expected

TABLE III. The TRK enhancement factor for INM, κ^{NM}, the isovector effective mass, m_v^*/m, and the ground state properties of ^{174}Yb obtained with various Skyrme EDFs. Note that $m_1(\hat{\mathcal{D}}_K)$ obtained with the double-commutator procedure, Eq. (21), is the same for the different values of the magnetic quantum number K.

Param.	κ^{NM}	m_v^*/m	^{174}Yb (g.s.)		
			$m_1(\hat{\mathcal{D}}_{K=0,\pm 1})$ $(e^2\text{fm}^2\text{MeV})$	κ^{IVD}	β
SkM*	0.5315	0.653	287.7	0.3973	0.312
SV-kap20	0.2	0.834	236.1	0.1466	0.337
SV-bas	0.4	0.715	266.5	0.2942	0.336
SV-kap60	0.6	0.625	297.1	0.4429	0.319

from the definitions of κ^{NM} and κ^{IVD} [9,39,44], the EWSR increases with the enhancement factor of INM; in other words, with the reduction of the isovector effective mass. The HFB ground states computed with three SV funtionals are similarly deformed. Thus, the density integration of Eq. (23) is also similar for all three functionals, yielding the common ratio of $\kappa^{IVD}/\kappa^{NM} \cong 0.74$.

In Fig. 6, IVD transition strengths obtained with SV-kap20, SV-bas, and SV-kap60 are plotted. One can clearly find that an increment of the enhancement factor leads to a shift of the IVD strength towards the higher energy region, as pointed out in Ref. [44] for the GDR of doubly-magic ^{208}Pb. Conversely, the shifted strength trivially yields an enhanced value due to its energy-weight in the EWSR. That is, if the isovector effective mass becomes lighter, the corresponding excitation energies becomes higher. This can be qualitatively explained within an analogy to the single-particle energies of the HO potential,
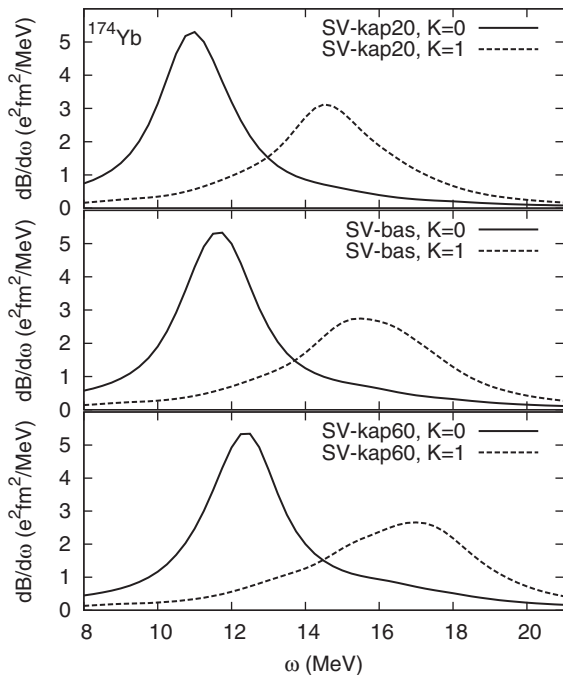

FIG. 6. Isovector dipole transition strength in ^{174}Yb, calculated with SV-kap20, SV-bas, and SV-kap60 parametrizations of Ref. [44].
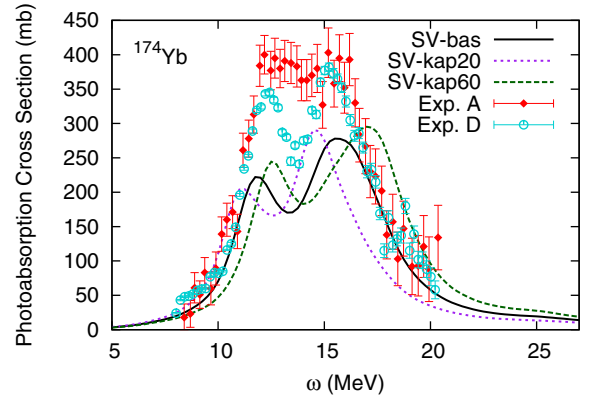

FIG. 7. Photoabsorption cross sections of ^{174}Yb calculated with SV-kap20, SV-bas, and SV-kap60 parametrizations. The shown experimental data are the same as in Fig. 3.

which have the same curvature, but different particle masses. From our calculations, the form of the ground state density is found to be insensitive to κ^{NM}. Thus, in this kind of case, the excitation energies are mainly determined by the effective mass for the collective motion.

The energy interval between the $K = 0$ and $K = 1$ peaks is not sensitive to κ^{NM}, due to similar deformation parameters listed in Table III. It is also noticeable that the total amplitude of the transition strength function is not significantly changed for different parametrizations, in both $K = 0$ and $K = 1$ cases. Thus, only the position of the peak is sensitive to κ^{NM}. From these results, we expect the mean frequency of GDR to be a suitable observable in order to constrain isovector effective mass parameter during EDF optimization.

The photoabsorption cross sections for SV-EDFs are plotted in Fig. 7. The shift of GDR structure to the high-energy region is again observed by the increase of κ^{NM}. The SV-kap20 functional reproduces the experimental data well up to $\omega = 11$ MeV, whereas the general structures match best to the SV-bas result, which corresponds to $\kappa^{NM} = 0.4$.

On the other hand, the GDR deficiency against the experimental data still remains: the calculated total photoabsorption cross section cannot be improved by changing the enhancement factor. In order to improve current EDF models, a parameter optimization, combined with an input data on the GDR position and magnitude, may help the situation.

IV. SUMMARY

We have performed a systematic analysis of the GDR in heavy rare-earth elements, including neutron-rich and deformed isotopes. The calculations were handled in the recently developed parallel FAM-QRPA scheme, in combination with the Skyrme EDF, without any additional truncations on the two-quasiparticle model space. This scheme enabled us to perform fully self-consistent QRPA calculations efficiently and free from the spurious effects due to the broken self-consistency.

The mean energy and width, as well as the plateau shape of the photoabsorption cross section, have been fairly well reproduced for nuclei considered. However, some deficiency

in the calculated total photoabsorption cross section was seen for $Z \geqslant 70$ isotopes.

We also investigated the behavior of GDR by changing the TRK enhancement factor, connected to the isovector effective mass. It is clearly shown that an increment of the enhancement factor shifts the GDR distribution towards the higher-energy region, corresponding to the lighter isovector effective mass.

The deficiency of GDR total photoabsorption cross section, with respect to the experimental data, remains an open question. This deficiency is noticeable in the region of isotopes heavier than Er. This situation could not be improved by tuning smearing width or κ^{NM}. Several possibilities of further improvements can be proposed. The first is to expand the framework to cover the dynamics beyond the QRPA, as well as the other multipole degrees of freedom. Especially, the octupole softness of systems could play a role at levels higher than the RPA. Another direction of progress is to perform a more systematic optimization of EDF parameters, and to use GDR data on deformed nuclei as an input. Especially, the tangled effect of the symmetry energy and its slope with the isovector effective mass is expected to be important [9,15,63].

Our FAM-QRPA scheme could be also employed to investigate the low-lying excitations or the pygmy strength. For the excitation energies as well as the partial sum rules of these resonances, not only the particle-hole part but also the pairing part of the EDF is expected to contribute notably. Especially for the low-lying excitations of loosely bound nuclei, the HFB method has an advantage over the BCS method for the treatment of pairing correlations, especially for nuclei close to the neutron drip line [64,65]. For this purpose, FAM-QRPA embedded into the coordinate-space HFB solver could be a good choice of method [30].

ACKNOWLEDGMENTS

[1] A. B. Migdal, J. Phys. (USSR) **8**, 331 (1944).
[2] M. Goldhaber and E. Teller, Phys. Rev. **74**, 1046 (1948).
[3] H. Steinwedel and J. H. D. Jensen, Z. Naturforsch. **5**, 413 (1950).
[4] M. N. Harakeh and A. van der Woude, *Giant Resonances: Fundamental High-Frequency Modes of Nuclear Excitation* (Oxford University Press, London, 2001).
[5] P. Ring and P. Schuck, *The Nuclear Many-Body Problems* (Springer-Verlag, Berlin, Germany, 1980).
[6] G. F. Bertsch and R. A. Broglia, *Oscillations in Finite Quantum Systems* (Cambridge University Press, Cambridge, UK, 1994).
[7] M. Arnould, S. Goriely, and K. Takahashi, Phys. Rep. **450**, 97 (2007).
[8] P.-G. Reinhard and H. Flocard, Nucl. Phys. A **584**, 467 (1995).
[9] P.-G. Reinhard, Nucl. Phys. A **649**, 305 (1999).
[10] B. L. Berman and S. C. Fultz, Rev. Mod. Phys. **47**, 713 (1975).
[11] D. Pena Arteaga, E. Khan, and P. Ring, Phys. Rev. C **79**, 034311 (2009).
[12] I. Daoutidis and S. Goriely, Phys. Rev. C **86**, 034328 (2012).
[13] K. Yoshida and T. Nakatsukasa, Phys. Rev. C **83**, 021304 (2011).
[14] K. Yoshida and T. Nakatsukasa, Phys. Rev. C **88**, 034309 (2013).
[15] W. Kleinig, V. O. Nesterenko, J. Kvasil, P.-G. Reinhard, and P. Vesely, Phys. Rev. C **78**, 044313 (2008).
[16] M. Matsuo, K. Mizuyama, and Y. Serizawa, Phys. Rev. C **71**, 064326 (2005).
[17] T. Oishi, K. Hagino, and H. Sagawa, Phys. Rev. C **84**, 057301 (2011).
[18] N. D. Dang and N. Q. Hung, J. Phys. G **40**, 105103 (2013).
[19] S. Ebata, T. Nakatsukasa, and T. Inakura, Phys. Rev. C **90**, 024303 (2014).
[20] S. Ebata, T. Nakatsukasa, and T. Inakura, Phys. Rev. C **92**, 049902(E) (2015).
[21] D. J. Dean and M. Hjorth-Jensen, Rev. Mod. Phys. **75**, 607 (2003).
[22] J. Terasaki and J. Engel, Phys. Rev. C **82**, 034326 (2010).

[23] J. Terasaki and J. Engel, Phys. Rev. C **84**, 014332 (2011).
[24] V. O. Nesterenko, J. Kvasil, and P.-G. Reinhard, Phys. Rev. C **66**, 044307 (2002).
[25] V. O. Nesterenko, W. Kleinig, J. Kvasil, P. Vesely, P.-G. Reinhard, and D. S. Dolci, Phys. Rev. C **74**, 064306 (2006).
[26] V. O. Nesterenko, W. Kleinig, J. Kvasil, P. Veselý, and P.-G. Reinhard, Int. J. Mod. Phys. E **17**, 89 (2008).
[27] T. Nakatsukasa, T. Inakura, and K. Yabana, Phys. Rev. C **76**, 024318 (2007).
[28] P. Avogadro and T. Nakatsukasa, Phys. Rev. C **84**, 014314 (2011).
[29] M. Stoitsov, M. Kortelainen, T. Nakatsukasa, C. Losa, and W. Nazarewicz, Phys. Rev. C **84**, 041305 (2011).
[30] J. C. Pei, M. Kortelainen, Y. N. Zhang, and F. R. Xu, Phys. Rev. C **90**, 051304 (2014).
[31] H. Liang, T. Nakatsukasa, Z. Niu, and J. Meng, Phys. Rev. C **87**, 054310 (2013).
[32] T. Nikšić, N. Kralj, T. Tutiš, D. Vretenar, and P. Ring, Phys. Rev. C **88**, 044327 (2013).
[33] T. Inakura, T. Nakatsukasa, and K. Yabana, Phys. Rev. C **80**, 044301 (2009).
[34] T. Inakura, T. Nakatsukasa, and K. Yabana, Phys. Rev. C **84**, 021302 (2011).
[35] P. Avogadro and T. Nakatsukasa, Phys. Rev. C **87**, 014331 (2013).
[36] M. T. Mustonen, T. Shafer, Z. Zenginerler, and J. Engel, Phys. Rev. C **90**, 024308 (2014).
[37] M. T. Mustonen and J. Engel, Phys. Rev. C **93**, 014304 (2016).
[38] N. Hinohara, M. Kortelainen, and W. Nazarewicz, Phys. Rev. C **87**, 064309 (2013).
[39] N. Hinohara, M. Kortelainen, W. Nazarewicz, and E. Olsen, Phys. Rev. C **91**, 044323 (2015).
[40] J. Toivanen, B. G. Carlsson, J. Dobaczewski, K. Mizuyama, R. R. Rodríguez-Guzmán, P. Toivanen, and P. Veselý, Phys. Rev. C **81**, 034312 (2010).

[41] P. Veselý, J. Toivanen, B. G. Carlsson, J. Dobaczewski, N. Michel, and A. Pastore, Phys. Rev. C **86**, 024303 (2012).

[42] B. G. Carlsson, J. Toivanen, and A. Pastore, Phys. Rev. C **86**, 014307 (2012).

[43] J. Dobaczewski and J. Dudek, Acta Phys. Pol. B **27**, 45 (1996).

[44] P. Klüpfel, P.-G. Reinhard, T. J. Bürvenich, and J. A. Maruhn, Phys. Rev. C **79**, 034310 (2009).

[45] E. Perlińska, S. G. Rohoziński, J. Dobaczewski, and W. Nazarewicz, Phys. Rev. C **69**, 014316 (2004).

[46] M. Kortelainen, T. Lesinski, J. Moré, W. Nazarewicz, J. Sarich, N. Schunck, M. V. Stoitsov, and S. Wild, Phys. Rev. C **82**, 024313 (2010).

[47] M. Kortelainen, N. Hinohara, and W. Nazarewicz, Phys. Rev. C **92**, 051302 (2015).

[48] D. D. Johnson, Phys. Rev. B **38**, 12807 (1988).

[49] A. Baran, A. Bulgac, M. M. Forbes, G. Hagen, W. Nazarewicz, N. Schunck, and M. V. Stoitsov, Phys. Rev. C **78**, 014318 (2008).

[50] J. Bartel, P. Quentin, M. Brack, C. Guet, and H.-B. Håkansson, Nucl. Phys. A **386**, 79 (1982).

[51] A. Pastore, D. Davesne, Y. Lallouet, M. Martini, K. Bennaceur, and J. Meyer, Phys. Rev. C **85**, 054317 (2012).

[52] M. Stoitsov, N. Schunck, M. Kortelainen, N. Michel, H. Nam, E. Olsen, J. Sarich, and S. Wild, Comput. Phys. Commun. **184**, 1592 (2013).

[53] P. Carlos, H. Beil, R. Bergère, A. Leprêtre, A. D. Miniac, and A. Veyssière, Nucl. Phys. A **225**, 171 (1974).

[54] G. M. Gurevich, L. E. Lazareva, V. M. Mazur, S. Y. Merkulov, G. V. Solodukhov, and V. A. Tyutin, Nucl. Phys. A **351**, 257 (1981).

[55] B. L. Berman, M. A. Kelly, R. L. Bramblett, J. T. Caldwell, H. S. Davis, and S. C. Fultz, Phys. Rev. **185**, 1576 (1969).

[56] B. I. Goryachev, Y. V. Kuznetsov, V. N. Orlin, N. A. Pozhidaeva, and V. G. Shevchenko, Yad. Fiz. **23**, 1145 (1976) [Sov. J. Nucl. Phys. **23**, 609 (1976)].

[57] A. M. Goryachev and G. N. Zalesnyy, Vopr. Teor. Yad. Fiz. **5**, 42 (1976).

[58] A. M. Goryachev and G. N. Zalesnyy, Yad. Fiz. **26**, 465 (1977) [Sov. J. Nucl. Phys. **26**, 246 (1977)].

[59] I. Stetcu, A. Bulgac, P. Magierski, and K. J. Roche, Phys. Rev. C **84**, 051309 (2011).

[60] D. J. Thouless, Nucl. Phys. **22**, 78 (1961).

[61] E. R. Marshalek and J. da Providência, Phys. Rev. C **7**, 2281 (1973).

[62] E. Khan, N. Sandulescu, M. Grasso, and N. V. Giai, Phys. Rev. C **66**, 024309 (2002).

[63] J. Piekarewicz, B. K. Agrawal, G. Colò, W. Nazarewicz, N. Paar, P.-G. Reinhard, X. Roca-Maza, and D. Vretenar, Phys. Rev. C **85**, 041302 (2012).

[64] J. Dobaczewski, H. Flocard, and J. Treiner, Nucl. Phys. A **422**, 103 (1984).

[65] A. Pastore, J. Margueron, P. Schuck, and X. Viñas, Phys. Rev. C **88**, 034314 (2013).